Journal of Materials Chemistry A

ROYAL SOCIETY OF CHEMISTRY

PAPER

View Article Online
View Journal | View Issue

Cite this: J. Mater. Chem. A, 2022, 10, 11542

Synthesis of photocatalytic pore size-tuned ZnO molecular foams†

Zachary Warren, Thais Tasso Guaraldo, Jannis Wenk and Davide Mattia *

The safe and efficient removal of organic micropollutants, such as pharmaceuticals, pesticides or caffeine from wastewater remains a major technological and environmental challenge. Here, the synthesis of self-supporting ZnO foam monoliths by direct incorporation of air into the forming gel is presented for the first time. These foams, labelled as MolFoams, showed a highly porous and interconnected structure, allowing for high solution flow rates and fast degradation kinetics of carbamazepine, a widely used pharmaceutical compound, used here as a model micropollutant. Altering the concentration of CTAB used in the formulation of the gels allowed controlling the size of the macropores of the MolFoam in the 0.69–0.84 mm range. Smaller macropores within the MolFoam structure were highly beneficial for the degradation of carbamazepine with pseudo first-order degradation kinetics of 5.43×10^{-3} min^{-1} for the MolFoams with the smallest macropore size. The best foams were tested in a recirculating reactor, with an optimal flow rate of 250 mL min^{-1}, resulting in a quantum yield of 0.69 and an electrical energy of 21.3 kW h m^{-3} per order, in addition to high mechanical and chemical stability. These results surpass the performance of photocatalytic slurries and immobilised systems, showing that self-supporting, photocatalytic foams can be an effective solution for the removal of organic micropollutants in wastewater.

Received 15th March 2022
Accepted 4th May 2022

DOI: 10.1039/d2ta02038f

rsc.li/materials-a

Introduction

The presence of organic micropollutants at ng L^{-1} to μg L^{-1} concentrations in water bodies poses an emerging threat to public health and aquatic ecosystems.[1,2] Organic micropollutants comprise a wide range of compounds including pesticides, pharmaceuticals, personal care products, drugs and hormones.[3] Many organic micropollutants cannot be efficiently removed with the physical, chemical and biological methods applied in conventional wastewater treatment plants.[4] Through wastewater effluent, organic micropollutants are discharged into the aquatic environment, where they exert ecotoxicological effects on aquatic organisms, bioaccumulate and eventually may reach water supplies or enter the human food chain.[5] New technology is required to effectively remove organic micropollutants during wastewater treatment. Advanced oxidation processes (AOPs) are among the most promising approaches for the removal of organic micropollutants in wastewater. AOPs encompass a wide range of different methods that utilize hydroxyl radicals as the main oxidizing species targeting organic micropollutants.[6] Ozone-based AOPs are widely used due to their low cost,[7] but can cause the formation of bromate compounds in water supplies with high concentrations of bromides, posing a risk to human health.[8] UV/H_2O_2 systems are also employed,[9] however the use of peroxide is limited by its low molar absorption coefficient, thereby requiring high concentrations to generate sufficient hydroxyl radicals.[10] Fenton related processes are less common, due to a low efficiency of the iron complexes when operated at the typical pH of wastewater.[6] The photocatalytic degradation of organic micropollutants has the potential to address some of the limitation of other AOPs,[11] but also faces some key challenges which have, so far, limited its large-scale adoption. Currently, photocatalysts are used as slurries or supported catalyst.[12] In slurries, suspensions of photocatalytic nanoparticles are mixed with the pollutant stream ensuring a high surface area contact between pollutant molecules and photocatalyst,[13] as well as a higher active surface area that can be irradiated.[14] A key drawback of photocatalytic slurries is the requirement for costly downstream separation of the slurry prior to release into waterways.[15] While the benefits of using nanoparticle slurries are significant, considerations need to be paid to the impacts of their release to the environment, with established evidence of bioaccumulation within fish, plants and mammals.[16] Furthermore, it has been shown that there is the potential for synergic interactions between catalyst nanoparticles and pollutants present in the environment, resulting in enhanced toxicity.[16] With supported catalysts downstream removal is not required as for slurries. However, supported catalysis have a lower surface area of catalyst in contact with the pollutant stream resulting in lower treatment

Department of Chemical Engineering, University of Bath, BA27AY, UK. E-mail: d.mattia@bath.ac.uk

† Electronic supplementary information (ESI) available. See https://doi.org/10.1039/d2ta02038f

efficiencies,[17,18] as well as issues of "shadowing", where the structure of the support and morphology of the catalyst can lead to areas where light cannot reach the surface, resulting in a reduced reactor efficiency.[18] Reticulated foam materials as supports for photocatalysts can integrate the advantages of supported immobilised catalysts with the higher surface areas of photocatalytic slurries. Synthesis of these generally involve decoration or coating a porous material, often Al_2O_3,[19] Ni[20] or SiC,[21] with photocatalytic nanoparticles, typically TiO_2,[19,22] or ZnO.[20] While these decorated foams have shown faster degradation kinetics than an equivalent unsupported catalyst,[19] they do not solve the issues associated with the potential leaching of nanoparticles in the treated wastewater.[23]

A further advancement in the use of foams has been to obtain a photocatalytically active porous monolithic structure, obtained from the sintering of ZnO microparticles around an organic template.[24] This approach removes the potential issue of weak adherence of particles to a support observed in decorated foams. However, zero leaching of particles cannot still be guaranteed during continued use. It is therefore advantageous to move away from the use of particles of any size in the synthesis, instead using a solution-based synthesis for the formation of monolithic photocatalysts.

Zinc oxide was selected as the starting metal oxide for this work, as its use as a photocatalyst in water treatment research is well established,[25] due to its UV active band gap of 3.2 eV, high electron mobility and low cost and toxicity.[26] Furthermore it absorbs over a wider range of wavelengths of light compared to TiO_2 allowing for greater utilisation of a light source and more efficient degradation of pollutants,[27] while additionally TiO_2 suffers from high rates of electron hole recombination which limits its effectiveness as a photocatalyst.[28] However ZnO is not without its drawbacks, including photo-corrosion under UV irradiation,[29] leading to the dissolution and formation of Zn^{2+} ions in solution, limiting its use for water treatment. The World Health Organisation limits the maximum concentration of Zn^{2+} in water to 3.0 ppm.[30] The impact of this photo-corrosion can be reduced at high dissolved oxygen concentration that stabilises ZnO.[31]

This work reports the use of a solution-based synthesis of zinc salt and a dicarboxylate linker in a sol–gel synthesis with controlled incorporation of air to form a porous zinc oxalate precursor foam, which is then sintered to form robust metal oxide foam. Synthesis in this manner has many advantages: firstly, the foams are produced avoiding the use of volatile foaming agents while still retaining the high porosity that would be expected from their synthetic use.[32,33] Furthermore, the sintering and conversion of oxalate to oxide results in a porous structure without the presence of discrete particles. Rather, a singular interconnected structure made of metal oxide is formed, thus removing the need for a porous support structure and discrete particles within the structure. As the formation of the porous monolith occurs *via* a bottom-up approach, using the reaction at a molecular basis, the foams synthesised in this way as called "Molecular Foams" or MolFoams.

Experimental

Materials

Zinc acetylacetonate (Zn $(AcAc)_2$; ≥95.0%), oxalic acid anhydrous (≥99.9%), hexadecyltrimethylammonium bromide (CTAB; ≥99.9%), polyethylene glycol (PEG; 10 000), ethanol (Absolute) and methylene blue were all purchased from Sigma Aldrich and used as provided. Jacketed, fritted funnels were purchased from Chemglass Lifesciences and fitted with PTFE sheets (Zwanzer). Desiccant from a Drierite™ gas-drying unit (Sigma Aldrich) was used as provided by the manufacturer but transferred to a smaller tube.

Synthesis of ZnO MolFoams

Zinc oxide foams were synthesised by substantially altering a method originally used to make nanoparticles,[34,35] to form a solid foam monolith (Fig. 1). First, $Zn(AcAc)_2$ (15.0 mmol) was added to a 25 mL Pyrex beaker. Subsequently, CTAB was dissolved in 15 mL ethanol and added to the beaker such that the final concentration in the reaction mixture was 5, 10, 15 or 20 mM respectively. Oxalic acid (15.0 mmol) and 40 μmol PEG10000 with 10 mL EtOH mixed in a separate beaker. Both solutions were stirred at 60 °C for 60 minutes in an oil bath until homogenous solutions were obtained. The solutions were sequentially added to a PTFE-lined, temperature controlled jacketed filter funnel at 60 °C. The reaction mixture was aerated with compressed air with an upward flow rate of 0.1 Standard Litres per Minute (sL min^{-1}) using a rotameter.

The reaction mixture of the Zn and acid solutions was aerated for 3 hours leading to the formation of a white gel. The gel was then transferred to a pre-weighed ceramic crucible and placed in a preheated muffle furnace (Carbolite CWF 1100) at 80 °C and dried for 12 hours to remove any remaining ethanol resulting in a dry zinc oxalate foam which was stored under ambient conditions.

Conversion of zinc oxalate foam into zinc oxide was achieved using a two-step thermal sintering process: the zinc oxalate foam was sintered using a furnace, heated to 1000 °C with a ramp rate of 5 °C min^{-1} and held at temperature for 0.5 hours, and then 900 °C with a ramp rate of 5 °C min^{-1} and held at temperature for 20 hours. This resulted in the formation of a mechanically stable ZnO foam. The high temperature sintering was also used to remove any remaining organic components. After sintering, the foams were cylindrical in shape, with an average diameter of 20 ± 1 mm and height of 19 ± 1 mm. Multiple parameters were studied, including sintering times and temperatures, aeration method, flow rate of air and composition of reactant solutions, for the formulation of the foams (Table S1†).

Characterisation of ZnO MolFoams

The surface morphology of the zinc oxide foams was studied using a JEOL 6301F FESEM and JEOL JSM-7900F FESEM. Prior to imaging, samples were coated with 20 nm Cr. The crystal structure of the foams was investigated using a STOE STADI P dual powder transmission X-ray diffractometer using a scanning range of $2\theta = 20$–$90°$ and a scan time of 20 minutes.

The chemical stability of the MolFoams was analysed using inductively coupled plasma mass spectrometry (ICP-MS) in a Thermo Fisher Scientific X-Series II instrument. All samples, standards and blanks, were spiked with internal standard elements Be, In, and Re. The Zn concentration was calibrated using six synthetic standards prepared from a 1000 ppm Inorganic Ventures (VA, USA) standard. The associated error was typically lower than 1.0%.

The porosity and internal structure of the MolFoam were determined using a combination of different characterisation methods. First, gravimetric porosity measurements were conducted using the Archimedes principle:[36]

$$\varepsilon = \frac{\omega_1 - \omega_2}{D_u} \Big/ \frac{\omega_1 - \omega_2}{D_u} + \frac{\omega_2}{D_f} \quad (1)$$

where ε is the porosity of the foam, ω_1 is the mass of the wet foam, ω_2 is the mass of the dry foam, D_u is the density of water (deionised, ultrapure) and D_f is the density of ZnO. The porosity and internal structure of the foams were further analysed using microcomputer tomography. The slices were collected using a Nikon XT H 225 ST using a 178 kV X-ray source and 0.708 s exposure time, 4 frames per projection and 3141 projections and analysed using Thermo Scientific AvizoSoftware 9 3D data visualisation software. This data was used to calculate the surface area : volume ratio, a_{vs}:[37]

$$a_{vs} = \frac{8.002\ \left(1 - 0.833\sqrt{1-\varepsilon}\right)}{d_p\sqrt{1-\varepsilon}} \quad (2)$$

where d_p is the pore diameter and ε is the porosity of the foam.

To probe the microporosity, the MolFoams were broken in smaller pieces and analysed *via* BET N2 adsorption using a Autosorb-iQ-C by Quantachrome Anton Paar at 77 K, after degassing under vacuum at 130 °C for 120 minutes, obtaining the specific surface area, SA_{BET}. Samples were loaded carefully avoiding the formation of powders, to avoid characterisation of the porosity of a powdered MolFoam.

Finally, a bespoke dyeing apparatus was developed to qualitatively assess the nature of the pores (open or closed porosity) within the MolFoam. A schematic of this can be found in Fig. S3.† Briefly, a solution of methylene blue (MB) was flowed through a tube (ID = 22 mm, OD = 25 mm) containing a MolFoam on a plastic support platform using a peristaltic pump (Masterflex L/S, pump head model 77200-62) operating at a flow rate of 50 mL min^{-1} for 120 minutes. After drying, the MolFoam was cut open showing sections dyed blue, indicative of open porosity, whereas sections left undyed would-be indicative of closed pores.

Photocatalytic reactor setup

For the reciculating photocatalytic experiments, reactor cartridges were made up of a quartz tube (h = 250 mm, OD = 25 mm, ID = 22 mm) with a 3D printed plastic buffer designed to hold the foams in place and prevent loss of the foam into the tubing and pump, positioned to avoid interference with the light source. A 3D model and a diagram of the reactor can be found in Fig. S1 and S2.†

ZnO MolFoams of known mass (0.7 g) were placed inside the cartridge and secured using subaseal fittings, connected to a gear pump (Ismatec, MCP-Z with a pump head Model GBS.P23.JVS.A-B1, Cole Parmer) connected to a jacketed beaker of 500 mL (acting as the reservoir) with a magnetic stirrer, where the temperature was maintained using a water-cooled bath (RC-10 Digital Chiller, VWR) with three UV lamps (Aquatix pond UV lamp, λ = 254 nm, 5 W) positioned equidistant around the quartz tube reactor containing the ZnO MolFoam at a distance of 3 cm served as the light source.

Photocatalytic activity (PCA) experiments

PCA experiments were conducted using 10 μM solutions of carbamazepine (CBZ) in 500 mL unbuffered ultrapure water at 10 ± 1 °C. CBZ was selected as a model micropollutant for photocatalytic activity (PCA) studies, due to its high UV stability,[38] and known degradation pathways,[39] allowing for comparison with both slurries and immobilised catalysts.[40,41] To minimize photocorrosion of ZnO,[31] CBZ solutions were saturated with O_2 for 40 minutes prior to experiments. The recirculating reactors were operated at flow rates between 100 mL min^{-1} and 500 mL min^{-1}. Control experiments were conducted in the absence of MolFoams in the reactor. Adsorption and removal of CBZ under dark conditions were found to be negligible as shown in Fig. S8.†

For all photocatalysis experiments, CBZ removal was monitored from 1 mL aliquots collected during sampling every 15 minutes for the first hour and every 30 minutes thereafter, such that the total volume removed was less than 10% of the starting reservoir volume, using high performance liquid chromatography (HPLC).

All experiments were repeated in triplicate. HPLC analysis of CBZ was performed on a Thermo Scientific Ultimate 3000 liquid chromatograph with a UV detector. CBZ analysis used a Thermo Scientific Acclaim 120 C_{18} column (3.0 × 75.0 mm, particle size 3.0 μm) and a Thermo Scientific Acclaim 120 C_{18} guard column (R) 120 C_{18} (3.0 × 10.0 mm, particle size 5.0 μm). The mobile phase was made up using 5.0 mM phosphoric acid and acetonitrile 70 : 30 (v/v) with a flow rate of 0.8 mL min^{-1}, injection volume of 20 μL and detection wavelength of 285 nm. Degradation of carbamazepine was measured *via* plotting (C_t/C_0) *vs.* time where C_0 is the initial concentration of CBZ and C_t is the concentration of CBZ at a given time. The pseudo first order degradation kinetics (k) was calculated *via* linear regression of a plot of $\ln(C_t/C_0)$ *vs.* time.

Photocatalyst quantum yields

The overall quantum yield ($\Phi_{overall}$) of a photocatalytic system is defined as the number of molecules of pollutant (carbamazepine) undergoing degradation relative to the number of photons reaching the catalyst surface.[42] The photon flux (E_{qf}) arriving at the surface of the photocatalyst along with the kinetic constant (k) allows calculating the overall quantum yield ($\Phi_{overall}$), assuming negligible photon loss due to scattering and all photons are absorbed by the photocatalyst:[43] Details of the calculations are provided in the ESI.†

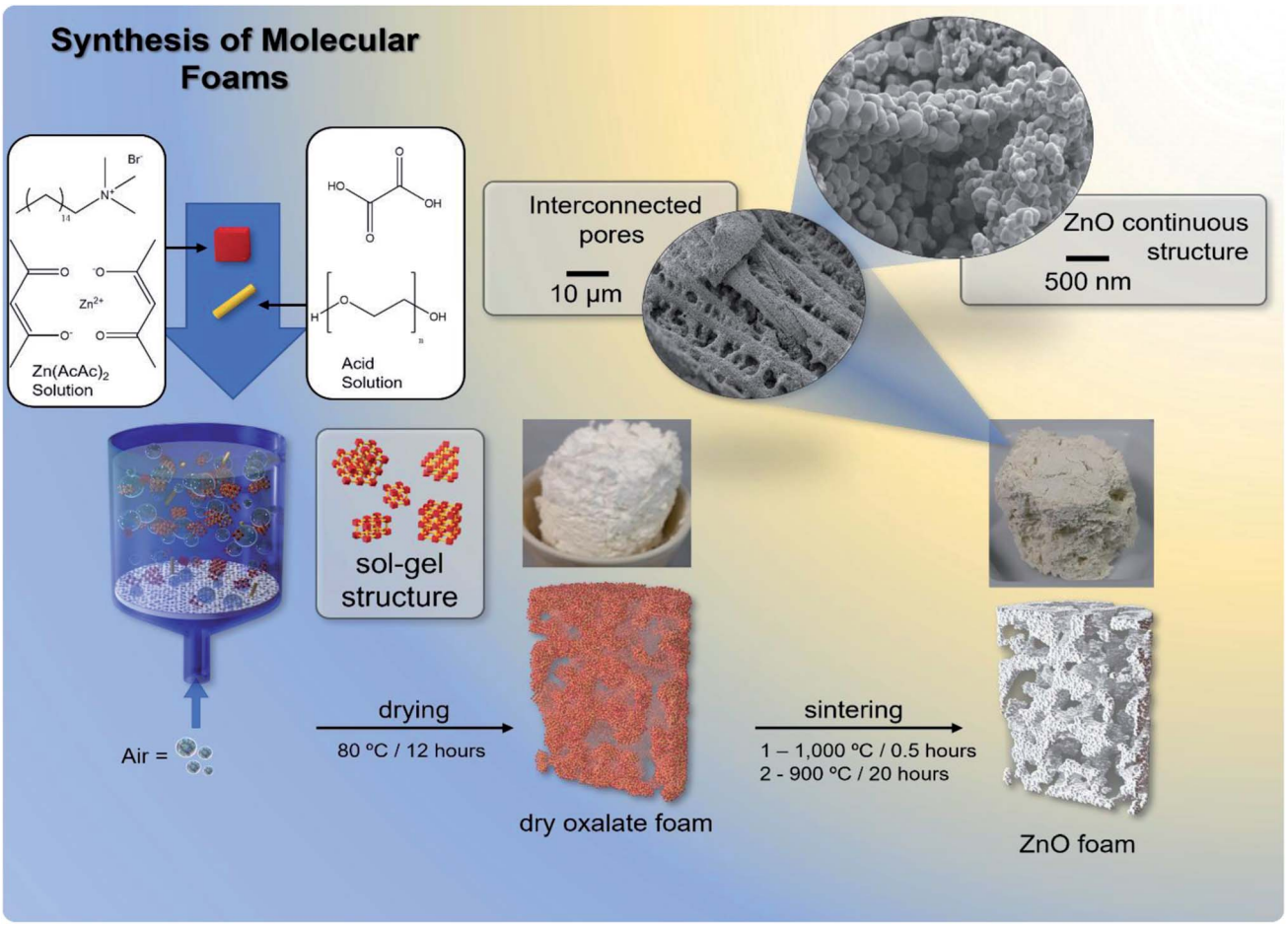

Fig. 1 Graphical overview of synthetic method of MolFoam production.

Electrical energy per order (E_{EO})

To assess the scale up potential of the system, the energy consumption of the reactor was estimated *via* the electrical energy per order (E_{EO}), defined as the kilowatt hour of electrical energy needed to decrease the concentration of a pollutant by an order of magnitude (90%) in one cubic metre of solution:[44]

$$E_{EO} = \frac{P \times t \times 1000}{(V)\left(\log \frac{C_0}{C_t}\right)} \quad (3)$$

where: P is the total power output of the 3 lamps onto the 12 cm long quartz tube, t is time in hours and V is the volume of the reservoir. As the foam occupied only a fraction of the quartz tube, the total power of the lamps was multiplied by the volumetric fraction occupied by the foam, to provide the effective power used for photocatalysis, considering that the contribution of photolysis is negligible. Details of the calculations are provided in the ESI.†

Results and discussion

ZnO MolFoams characterisation

Upon removal from the funnel, the wet gel monoliths were white in colour, free-standing and plastic *via* gentle pressure. After drying, the samples became brittle upon application of pressure. The dried monoliths were 28 mm in diameter and 30 mm in height on average. This decreased to 20 ± 1 mm diameter and 19 ± 1 mm height post sintering and could be handled and subjected to flow experiments.

The XRD pattern of the foams (Fig. S4†) shows the formation of hexagonal wurtzite ZnO with lattice parameters of $a = b =$ 3.25 Å and $c =$ 5.21 Å, sharp peaks indicating the sample is highly crystalline in nature and strongest intensity in the peaks associated with the (100), (002) and (101) crystal phases. All peaks are in agreement with those reported from JCPDS no. 36-1451.[45] The gravimetric porosity of these MolFoams, as measured using the Archimedes principle,[36] was found in all cases to be 95 ± 1%. This high porosity is required for solution flow through the foams in a flow reactor system. Furthermore, this high porosity is comparable with those reported in the literature for metal oxide aerogels,[46,47] with the key distinction that this porosity is achieved without the use of volatile foaming agents such as propylene oxide, nor the use of supercritical CO_2 (sCO_2). The FESEM micrographs show the presence of interconnected pores with faceted wall structures within the foam (Fig. 2). The MicroCT slices and 3D reconstructions (Fig. S5†) show the internal structure of the MolFoams to be comprised of irregularly shaped pores and channels, connecting throughout

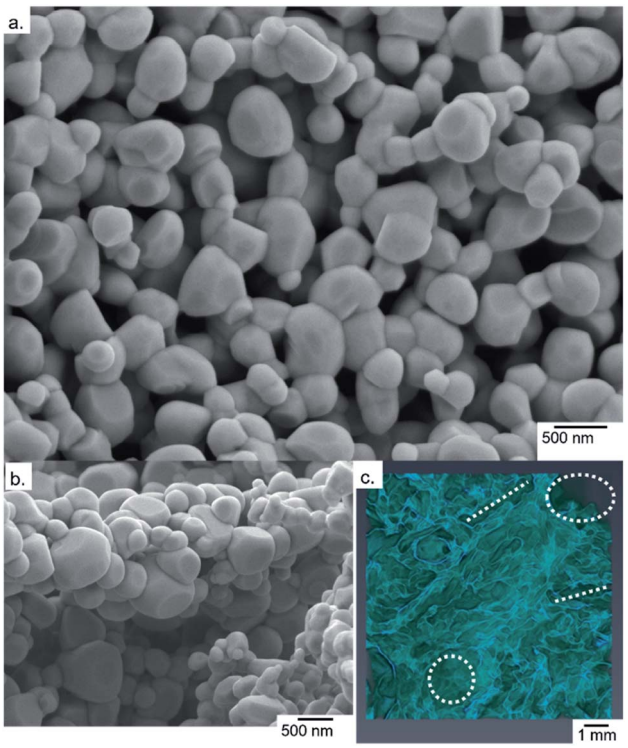

Fig. 2 FE-SEM micrographs showing the interconnected structure of the MolFoams (a) and the irregular microporous channel structure (b). (c) 3D reconstruction from MicroCT showing the irregular pore and channel structures within the MolFoams. The dashed circles and lines highlight examples of pores and channels, respectively.

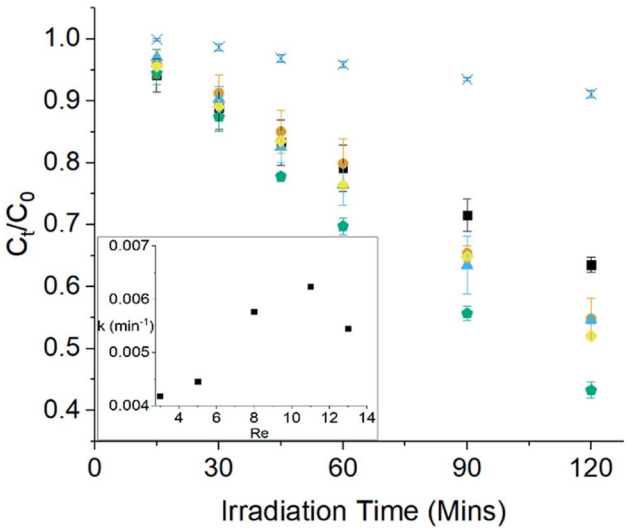

Fig. 3 Photocatalytic degradation of CBZ using ZnO MolFoams at varying flow rates × photolysis, ■ 100 mL min^{-1}, ● 200 m L min^{-1}, ▲ 300 mL min^{-1}, ⬟ 400 mL min^{-1}, ◆ 500 mL min^{-1}. Inset shows first order reaction kinetic as a function of flow rate (Reynolds number).

the MolFoam. The irregularity of the pores can be ascribed to multiple factors: The use of EtOH as a solvent resulted in CTAB concentration well below the critical micelle concentration (CMC) of the CTAB/EtOH system of 0.24 M,[48] hindering formation of regular micelles compared to an equivalent system using an aqueous solvent; and the densification due to sintering, compounded by the release of CO_2 from the zinc structures during the conversion of the oxalate into the oxide.[34]

Effect of flow rate on photocatalytic activity of MolFoams synthesised using 5 mM CTAB solution

The photocatalytic activity of the MolFoam was investigated in a recirculating flow reactor. Initially operated at 100 mL min^{-1} in the absence of a MolFoam, the carbamazepine underwent minimal degradation (9%) within 2 hours due to photolysis alone. When the ZnO MolFoam photocatalyst was added, the degradation increased to 36% after 2 hours (Fig. 3). Further increases of the flow rate from 100 to 400 mL min^{-1}, led to an increase in the total degradation of CBZ to 57% (Fig. 3). This increase in CBZ removal, along with a corresponding increase in kinetics reveals that the process is in the mass transfer limited regime, a well reported effect wherein the diffusion of pollutant through the boundary layer at the catalyst/pollutant interface limits the rate of degradation.[49] As the flow rate is increased, this leads to the formation of a thinner boundary layer at the catalyst surface between it and the bulk of solution, reducing the time required for the carbamazepine molecules to diffuse to the surface of the foams.[12] The effect of this can be seen clearly within Fig. 3, where, as the flow rate is increased, both the degradation of carbamazepine and the kinetics increase, with a significant change in the kinetics between 200 and 300 mL min^{-1}. The change becomes less pronounced as the flow rate is further increased and begins to decrease at flow rates of 500 mL min^{-1}. Comparable phenomena has been observed for the photocatalytic degradation of phenol using ZnO wire.[31] However whether this is indicative that the system is no longer in the mass transfer-limited regime and the adsorption of carbamazepine onto the ZnO is the rate limiting factor is unclear, as it was at this high flow rate that the foams underwent significant mechanical degradation and, hence, were deemed unsuitable for use at these higher flowrates. As such the MolFoams were modified to improve their mechanical stability at higher flow rates.

Furthermore, the quantum yields of these MolFoams ranged from 0.32 to 0.48 at flow rates of 100 and 400 mL min^{-1}, respectively. While these initial values are higher than for those reported for supported TiO_2,[50,51] and comparable with ZnO nanoparticle slurries,[41,52] they are lower than those for other ZnO foams.[24] Further comparisons with quantum yields reported in the literature can be found in Table S8.† In a practical sense this shows that between 50 and 70% of the photons emitted by the UV source are not used in the degradation of carbamazepine leading to low efficiencies of the reactor.

CTAB-modified MolFoams

The concentration of CTAB in the formulation was modified to increase the mechanical stability of the MolFoams at higher flowrates. Initially, CTAB was used as a surfactant solely to stabilise the air bubbles within the gel and increase the porosity of the foams.[53,54] It was then theorised that by increasing the

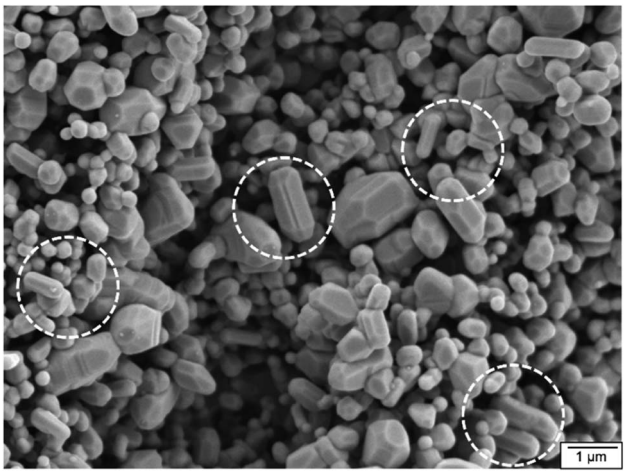

Fig. 4 FE-SEM micrograph of ZnO MolFoams synthesised using 10 mM CTAB solutions. Encircled regions show highly faceted rod-like structures.

concentration of the surfactant, the foams would be able to incorporate more air and show both greater porosity and larger pore sizes, as greater stabilisation of the air/EtOH interface occurs. Small increases to the CTAB concentration were made, to achieve final concentrations of CTAB in the foams of either 5, 10, 15 or 20 mM, still well below the CMC. Foams synthesised with the increased CTAB concentrations up to 15 mM showed no change in macroscopic dimensions, while the foams synthesised using 20 mM CTAB were slightly squatter than previous foams. At the microstructural level, on the other hand, there were significant changes: the increased presence of the CTAB led to the formation of more rod-like microstructures within the foam structure (Fig. 4and S6†) with a higher proportion of the crystals showing well-defined facets.

This combination has been shown to result in higher photocatalytic activity,[55] due to these facets showing greater potential for adsorption of pollutants to the surface, as well as showing greater trapping of photoexcited electrons and holes at the surface.[56] ZnO nanorods are well reported to have increased charge separation and trapping properties, associated with the higher aspect ratio of the crystals compared with other morphologies as this leads to greater delocalisation of electrons.[57] Furthermore the [002] crystal plane and associated (0001) facet have been shown to promote adsorption of oxygen species, allowing for the formation of reactive hydroxyl radicals to promoted degradation of pollutant species.[58] The formation of the rod-like structures is attributed to the preferential adsorption of ionic surfactants on the [100] crystal plane or (1010) crystal facet, which, in turn, has an inhibitory effect on the crystal growth in this direction.[59,60] This then promotes growth of the crystal along the [101] crystal plane of the (1011) facet,[59] and the [002] plane of the (0001) facet,[61] resulting in the formation of the longer rod-like structures observed here and in the literature.[62]

It is widely reported that particle shape has a significant impact on the photocatalytic activity of ZnO, along with the effect the shape has on the relative intensity of the main ZnO peaks within the XRD,[45] in particular, regarding ZnO nanorods as increasing the CTAB concentration from 5 to 10 mM lead to an increase in the relative intensity of the (100), (002) and (101) peaks, suggesting a degree of crystallite anisotropy,[60] while a decrease in relative intensity of the (100)/(101) ratio from 0.70 to 0.65 and (002)/(101) ratio from 0.50 to 0.44 is indicative of an increased presence of 1011 facets typical of those found on ZnO rod-like structures.[55] Further increases in the CTAB concentration did not lead to any further changes in the relative intensities or ratio of the peak intensities, indicating no further changes to the shape of the crystallites, with similar findings reported in the literature.[61]

The degradation of CBZ and the degradation kinetics follow a nonlinear relationship, with the Pearson's r value for the correlations between CTAB concentration and degradation or kinetics being only 0.33 and 0.18, respectively (Table 1). Fig. 5a shows that the highest kinetics and greatest CBZ removal occurring in MolFoams synthesised using 10 mM CTAB solutions, increasing from 5 mM and then decreasing as the concentration increases further.

This suggests that, while 10 mM is the optimum CTAB concentration, the greater concentration of CTAB is not directly responsible for this increase, nor is it the increased presence of the rod-like crystals that are observed at higher concentrations. It is likely that this increased activity is due to the effect that the

Table 1 Correlation between [CTAB], CBZ removal for foams prepared at different CTAB conditions (120 min irradiation time, flow rate 200 mL min^{-1}) and pseudo first order degradation kinetics (k) with the porosity calculated by Archimedes' method (e), macropore diameter and pore surface area : volume ratio (a_{vs}) and BET surface (SABET). Also tabulated are overall quantum yield ($\Phi_{overall}$) and E_{EO} at corresponding CTAB concentrations

[CTAB]/mM	C_{120}/C_0	k ($\times10^{-3}$)/min^{-1}	ε/%	Macropore diameter/mm	a_{vs}/cm^{-1}	SA_{BET}/m^2 g^{-1}	$\Phi_{Overall}$	E_{EO}/kW h m^{-3}
5	0.56 ± 0.03	4.44 ± 0.32	96	0.81 ± 0.02	16.50	34.50	0.34	39.7 ± 3.9
10	0.48 ± 0.02	5.43 ± 0.37	96	0.69 ± 0.01	19.37	35.68	0.41	31.4 ± 1.9
15	0.53 ± 0.03	5.29 ± 0.17	96	0.76 ± 0.01	17.58	28.18	0.40	36.3 ± 3.4
20	0.58 ± 0.02	4.71 ± 0.18	94	0.84 ± 0.02	15.91	39.05	0.36	42.3 ± 2.8
Correlation	0.33	0.18	−0.78	0.32	−0.30	0.17		
	Correlation – kinetics		0.37	−0.85	0.85	−0.41		
	Correlation – degradation		−0.65	0.99	−0.99	0.29		

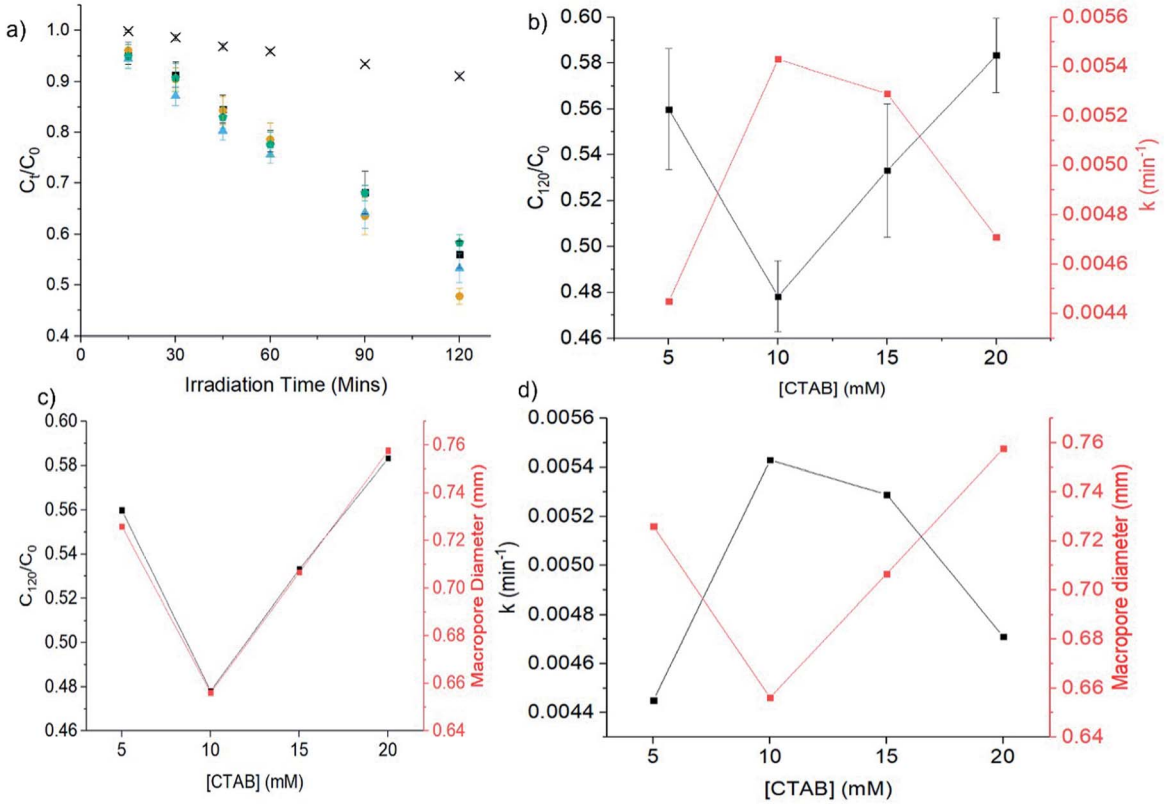

Fig. 5 (a) Photocatalytic degradation of CBZ using ZnO MolFoams synthesised using various CTAB concentrations: × photolysis, ■ 5 mM, ● 10 mM, ▲ 15 mM, ⬟ 20 mM. Relationship between [CTAB] and (b) CBZ degradation and the associated pseudo first order kinetics; (c) CBZ degradation and the pore diameter of the MolFoams; and (d) pseudo first order kinetics and the pore diameter of the MolFoams.

CTAB has on the structural properties of the MolFoams. As the CTAB concentration increases, the average diameter of the pores shows a minimum macropore size for 10 mM CTAB, then increasing as the concentration increases, while at minimum pore diameter, the degradation and reaction kinetics are highest (Fig. 5b–d). This is further reinforced by the Pearson's r value for the correlations for macropore size and the related SA/V ratio of the pores with very strong correlation to the degradation of carbamazepine ($r = 0.99$ and -0.99, respectively) and strong correlation with the pseudo first order kinetics ($r = -0.85$ and 0.85, respectively) as shown in Table 1. The decrease in pore size can be qualitatively observed in Fig. 6c and d, where the 3D reconstruction of the MolFoams shows the formation of smaller pores in the foams synthesised with higher CTAB concentrations. This is of particular interest as opinion within the literature is divided on the impact of pore size on the degradation activities of supported catalysts. One argument is that the smaller the pore size, the higher the surface areas within,[63] resulting in larger reactive catalyst area. This, along with thinner coatings of catalyst allows for greater light utilisation.[37] A contrasting argument is that the larger the pore size, the greater the light penetration into the foam and thus greater activation of photocatalyst.[64] However, this argument is frequently made of foams of photocatalytically inactive materials such as alumina with thick struts surrounding the pores.[65,66] Larger pores also offer less resistance to the flow of the solution through the foam structure.[65] Fig. 5 shows a clear relationship between CTAB concentration and the pore size of the foams as well as the degradation of CBZ and reaction kinetics, with the smaller pore sizes leading to greater degradations and higher kinetic constants. The improved activity from smaller pores can be explained by the hierarchical pore structure of the foams. The channels within the foam favour fluid flow through the porous material, while the smaller macropores, as observed in the 10 mM CTAB samples, provide greater degradations and higher kinetics, due to pollutant molecules having shorter diffusion times within smaller pores.[49] Reducing the macropore size increases the rate of diffusion, resulting in faster kinetics and higher degradation of CBZ. Smaller pores also provide higher surface areas for the degradation reaction to occur. Furthermore, the reduction of pore size without changes in overall porosity suggests the presence of a greater number of pores within the foam structure with each individual pore having a higher surface area: volume ratio and acting as a site for the adsorption and degradation of pollutant molecules from the eluent stream.

Effect of flow rate on photocatalytic activity of 10 mM CTAB MolFoams

As shown in Table S4,† increasing the flow rate of the reactor leads to an increase in the quantum yield of the system. As such, the photocatalytic activity of the 10 mM CTAB synthesised

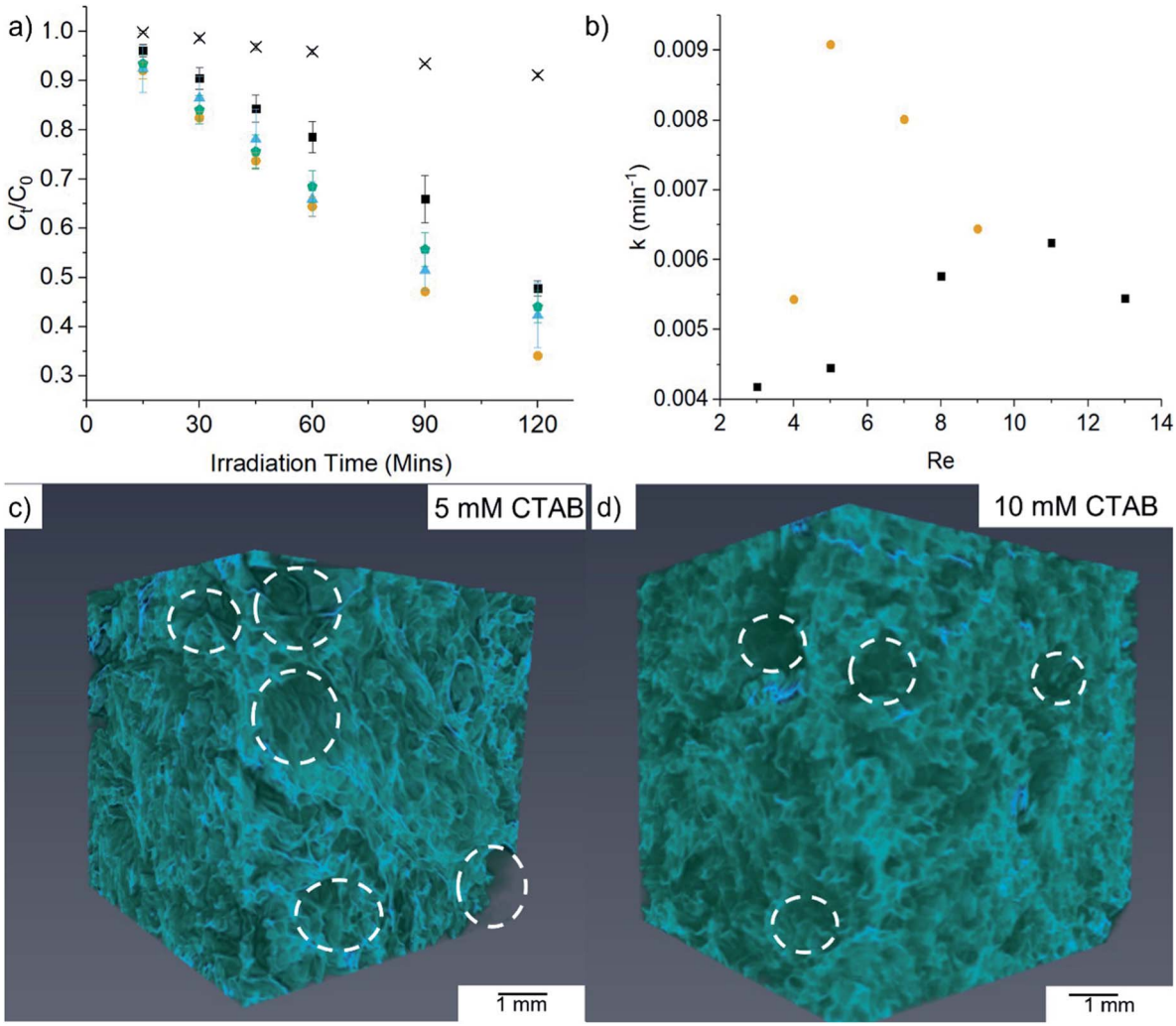

Fig. 6 (a) Photocatalytic degradation of CBZ using MolFoams synthesised using 10 mM CTAB within a recirculating reactor operated at various flow rates [x photolysis ■ 200 mL min^{-1}, ● 250 mL min^{-1}, ▲ 300 mL min^{-1}, ⬟ 400 mL min^{-1}]. (b) First order kinetic constant for MolFoams synthesised using ■ 5 mM, ● 10 mM CTAB as a function of flow rate (Reynolds number) (c and d) MicroCT 3D reconstructions of MolFoams synthesised using 5 or 10 mM CTAB solutions, respectively. Circled areas highlight the decrease in pore size as CTAB concentration increases.

MolFoams was evaluated within the recirculating reactor at flow rates between 200- and 400 mL min^{-1} (Fig. 6a). The degradation increases as the flow rate is increased, with the highest removal of CBZ occurring at 250 mL min^{-1}. The 10 mM CTAB synthesised foams show faster kinetics than the 5 mM MolFoams operated at the same flow rate (Fig. 6b). This is attributed to the improvements in activity promoted by the reduction in pore size and larger surface area-to-volume ratio within the pores that occurs with the use of higher CTAB concentrations. Of particular interest is the variation in the profiles in Fig. 6b, with the 10 mM CTAB MolFoams showing an optimum flow rate of 250 mL min^{-1} compared to 400 mL min^{-1} for the 5 mM MolFoams. The corresponding kinetics at the optimal flow rate of the 10 mM system are around 150% that of the 5 mM system. Furthermore, changes in the flow rate for the 10 mM MolFoams have a greater effect on the kinetics with the profile showing a much sharper peak for the 10 mM system, compared with the gradual increase and decrease of the kinetics seen in the 5 mM. This suggests that the increase in the flow rate within the 10 mM system and the reduction of the boundary layer thickness has a more pronounced impact on the kinetics. This behaviour can be effectively explained by the presence of more smaller pores,[63] as discussed earlier.

This analysis is further confirmed by hydrodynamic calculations for the reactor system, showing a Peclet number (ratio of convective to diffusional mass transfer) significantly greater than 1, and a more than doubling of the Sherwood number (ratio of convective mass transfer rate to the rate of diffusive mass transfer) from 4 to 9 as the flow rate of the system increases. Both confirm that the higher flow rates used lead to higher rates of convective mass transfer within the reactor,[31] overcoming mass transfer resistances (Table S5†). The E_{EO} of the foam reactor system is reduced in all cases, when compared to equivalent flow rates using 5 mM CTAB foams (Table S4†). As can be seen in Fig. 7, operating the reactor using a 10 mM CTAB foam with the flow rate of 250 mL min^{-1} provides the best

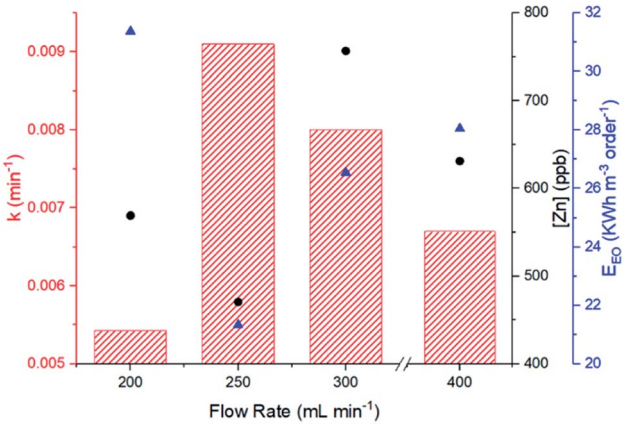

Fig. 7 Comparison between ● zinc concentration post photocatalytic CBZ degradation after 120 min, pseudo first order reaction kinetics (bar) and ▲ E_{EO} of MolFoam reactors operating at various flow rates.

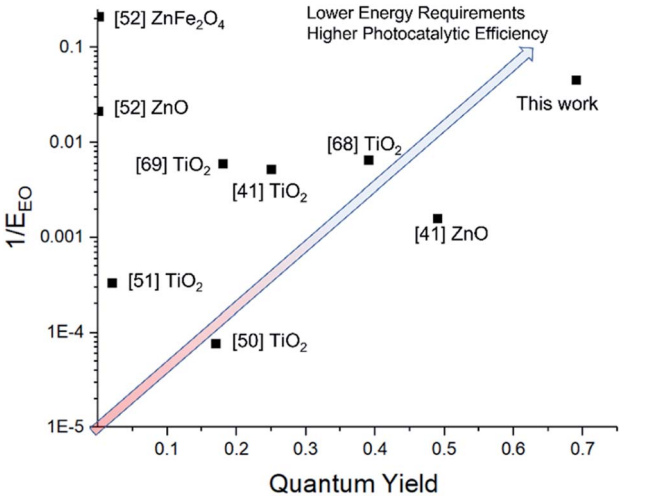

Fig. 8 Plot mapping quantum yield and log of $1/E_{EO}$ of photocatalytic systems for the degradation of CBZ.

overall performance within the range studied in terms of kinetics, zinc concentration and E_{EO}. Furthermore, as tabulated in Table S5,† the optimisation of both the MolFoams, through control of macropore size *via* CTAB concentration, and the reactor, through control of the flow rate, leads to an increase of the quantum yield from an initial value of 0.34 up to a maximum of 0.69, showing a significant increase in photocatalytic efficiency. This, coupled with the electrical energy per order (E_{EO}) of the reactors decreasing by over 50%, means the optimised foam/reactor system requires less than half the electrical energy relative to those initially tested, showing promise for scale up.

Additionally, all zinc concentrations after photocatalytic degradations show levels in the ppb range, significantly lower than the WHO limits of 3.0 ppm.[30] The FE-SEM micrographs in Fig. S7† show no appreciable change in the morphology at a range of magnifications of the MolFoams after photocatalytic degradation corroborates this and further reinforces the chemical stability of the MolFoam structure. A comparison with other photocatalytic systems for the degradation of CBZ shows that the MolFoam outperform reported literature in terms of energy requirements, *i.e.* lowest E_{EO}, and photocatalytic efficiency, *i.e.* highest quantum yield (Fig. 8 and Table S8†). This included TiO_2 and ZnO photocatalysts, batch nanoparticle slurries systems,[67–69] and supported catalysts in recirculating or flow systems.[40,51,68] In some instances, the catalysts showed higher kinetics but lower overall quantum yields and higher electrical energy per order values, highlighting the advantages of the highly porous and interconnected structure of the MolFoams. It is noted here that while there is a vast literature on the photocatalytic degradation of CBZ, direct comparisons are challenging due to lack of essential details on the quantum yield, *e.g.* light intensity,[43] or energy requirements, despite these being considered best practise for the field.[70] This is often due to a focus on kinetics, which favour nanoparticle slurries,[41,68] whereas quantum yield and energy requirements are more useful when considering the potential practical use of photocatalysts. In this context, a treatment system that makes use of a MolFoam will be able to provide comparable or better photocatalytic activity and removal of pollutants, with greater photocatalytic efficiency and lower energy requirements, while removing the need for the downstream removal required for slurries.

Conclusions

Porous ZnO monoliths, defined here as MolFoams, were synthesised through a novel process which results in a continuously interconnected structure with no discrete nano- or microparticles, a major advancement compared to other foams used for photocatalysis. MolFoams were synthesised using a range of concentrations of CTAB leading to changes in the morphology and pore structure of the foams. While initial MolFoams using 5 mM CTAB lost integrity at the higher flow rates needed to overcome mass transfer resistance, those prepared using 10 mM CTAB showed the greatest degradation of carbamazepine at all flow rates. Changes in the morphology induced by the higher CTAB concentration, with a smaller average macropore size, resulted in the highest degradation kinetics of 0.009 min^{-1} occurring at a lower flow rate of 250 mL min^{-1}, with high mechanical and chemical stability. Furthermore, when considering the energy requirements and the photocatalytic efficiency, *via* the electrical energy per order and quantum yield, respectively, the MolFoams outperformed both immobilised and slurry systems, in batch and in flow for a variety of photocatalysts. This can be attributed to the highly porous and interconnected structure of the MolFoams which enables high light penetration with short diffusion paths for the pollutant to reach the catalyst surface. All these characteristics show that the MolFoams have the potential to overcome the limits of current photocatalytic systems which have so far limited their practical use, providing a safe and viable method for the removal of organic micropollutants from wastewater.

Data availability

Data supporting this work is freely accessible in the Bath research data archive system at **https://doi.org/10.15125/BATH-01118**.

Author contributions

Zachary Warren: conceptualisation, investigation, methodology, validation, visualisation, writing – original draft. Thais Tasso Guaraldo: conceptualisation, writing – review & editing. Jannis Wenk: conceptualisation, supervision, writing – review & editing. Davide Mattia: conceptualisation, funding acquisition, project administration, resources, supervision, writing – review & editing.

Conflicts of interest

There are no conflicts to declare.

Acknowledgements

The authors would like to acknowledge the EPSRC for funding (EP/P031382/1). ZW acknowledges The University of Bath for funding his PhD ZW would also like to acknowledge R. Castaing, P. Fletcher, D. Lednitzky and S. Reeksting of MC^2 University of Bath analytical facilities, G. Kociok-Köhn of Department of Chemistry and J. A. Milton of The National Oceanography Centre Southampton for support and assistance in collection of the data presented here. The authors also acknowledge D. F. Segura for artwork support.

References

1 J. K. Fawell, *Water Sci. Technol.*, 2008, **57**, 183–187.
2 T. Reemtsma, S. Weiss, J. Mueller, M. Petrovic, S. Gonzalez, D. Barcelo, F. Ventura and T. P. Knepper, *Environ. Sci. Technol.*, 2006, **40**, 5451–5458.
3 J. Virkutyte, R. S. Varma and V. Jegatheesan, *Treatment of Micropollutants in Water and Wastewater*, IWA Publishing, 2010.
4 A. Joss, S. Zabczynski, A. Göbel, B. Hoffmann, D. Löffler, C. S. McArdell, T. A. Ternes, A. Thomsen and H. Siegrist, *Water Res.*, 2006, **40**, 1686–1696.
5 K. Fent, A. A. Weston and D. Caminada, *Aquat. Toxicol.*, 2006, **76**, 122–159.
6 Y. Deng and R. Zhao, *Curr. Pollut. Rep.*, 2015, **1**, 167–176.
7 Y. Luo, W. Guo, H. H. Ngo, L. D. Nghiem, F. I. Hai, J. Zhang, S. Liang and X. C. Wang, *Sci. Total Environ.*, 2014, **473–474**, 619–641.
8 U. von Gunten and J. Hoigné, *Environ. Sci. Technol.*, 1994, **28**, 1234–1242.
9 D. B. Miklos, C. Remy, M. Jekel, K. G. Linden, J. E. Drewes and U. Hubner, *Water Res.*, 2018, **139**, 118–131.
10 G. V. Buxton, C. L. Greenstock, W. P. Helman and A. B. Ross, *J. Phys. Chem. Ref. Data*, 1988, **17**, 513–886.
11 C. Martínez, M. L. Canle, M. I. Fernández, J. A. Santaballa and J. Faria, *Appl. Catal., B*, 2011, **102**, 563–571.
12 H. d. Lasa, *Photocatalytic Reaction Engineering*, Springer, Boston, MA, 2005.
13 C. Yu, W. Zhou, H. Liu, Y. Liu and D. D. Dionysiou, *Chem. Eng. J.*, 2016, **287**, 117–129.
14 A. Manassero, M. L. Satuf and O. M. Alfano, *Chem. Eng. J.*, 2017, **326**, 29–36.
15 P. Fernández-Ibáñez, S. Malato and F. J. de las Nieves, *Catal. Today*, 1999, **54**, 195–204.
16 B. Nowack and T. D. Bucheli, *Environ. Pollut.*, 2007, **150**, 5–22.
17 M. F. J. Dijkstra, A. Michorius, H. Buwalda, H. J. Panneman, J. G. M. Winkelman and A. A. C. M. Beenackers, *Catal. Today*, 2001, **66**, 487–494.
18 M. Bideau, B. Claudel, C. Dubien, L. Faure and H. Kazouan, *J. Photochem. Photobiol., A*, 1995, **91**, 137–144.
19 I. J. Ochuma, O. O. Osibo, R. P. Fishwick, S. Pollington, A. Wagland, J. Wood and J. M. Winterbottom, *Catal. Today*, 2007, **128**, 100–107.
20 Y. F. Zhu, L. Zhou and Q. S. Jiang, *Ceram. Int.*, 2020, **46**, 1158–1163.
21 N. A. Kouamé, D. Robert, V. Keller, N. Keller, C. Pham and P. Nguyen, *Catal. Today*, 2011, **161**, 3–7.
22 N. A. Kouame, D. Robert, V. Keller, N. Keller, C. Pham and P. Nguyen, *Environ. Sci. Pollut. Res. Int.*, 2012, **19**, 3727–3734.
23 C. B. Ong, L. Y. Ng and A. W. Mohammad, *Renewable Sustainable Energy Rev.*, 2018, **81**, 536–551.
24 T. Tasso Guaraldo, J. Wenk and D. Mattia, *Adv. Sustainable Syst.*, 2021, **5**, 2000208.
25 D. Maučec, A. Šuligoj, A. Ristić, G. Dražić, A. Pintar and N. N. Tušar, *Catal. Today*, 2018, **310**, 32–41.
26 J. S. Chang, J. Strunk, M. N. Chong, P. E. Poh and J. D. Ocon, *J. Hazard. Mater.*, 2020, **381**, 120958.
27 R. Qiu, D. Zhang, Y. Mo, L. Song, E. Brewer, X. Huang and Y. Xiong, *J. Hazard. Mater.*, 2008, **156**, 80–85.
28 N. M. Gupta, *Renewable Sustainable Energy Rev.*, 2017, **71**, 585–601.
29 K. M. Lee, C. W. Lai, K. S. Ngai and J. C. Juan, *Water Res.*, 2016, **88**, 428–448.
30 UNICEF, *WHOUNICEF-Joint-Monitoring-Program-for-Water-Supply-Sanitation-and-Hygiene-JMP*, 2017, **https://www.unwater.org/publications/whounicef-joint-monitoring-program-water-supply-sanitation-hygiene-jmp-2017-update-sdg-baselines/**.
31 C. M. Taylor, A. Ramirez-Canon, J. Wenk and D. Mattia, *J. Hazard. Mater.*, 2019, **378**, 120799.
32 X. Lu, K. Kanamori and K. Nakanishi, *New J. Chem.*, 2019, **43**, 11720–11726.
33 O. Durupthy, M. Jaber, N. Steunou, J. Maquet, G. T. Chandrappa and J. Livage, *Chem. Mater.*, 2005, **17**, 6395–6402.
34 K. G. Kanade, B. B. Kale, R. C. Aiyer and B. K. Das, *Mater. Res. Bull.*, 2006, **41**, 590–600.
35 S. Thota, T. Dutta and J. Kumar, *J. Phys.: Condens. Matter*, 2006, **18**, 2473–2486.

36 Y. Liao, R. Wang, M. Tian, C. Qiu and A. G. Fane, *J. Membr. Sci.*, 2013, **425–426**, 30–39.
37 D. Hao, Z. Yang, C. Jiang and J. Zhang, *Appl. Catal., B*, 2014, **144**, 196–202.
38 F. Ali, J. A. Khan, N. S. Shah, M. Sayed and H. M. Khan, *Process Saf. Environ. Prot.*, 2018, **117**, 307–314.
39 J. Zhai, Q. Wang, Q. Li, B. Shang, M. H. Rahaman, J. Liang, J. Ji and W. Liu, *Sci. Total Environ.*, 2018, **640–641**, 981–988.
40 V. Rogé, C. Guignard, G. Lamblin, F. Laporte, I. Fechete, F. Garin, A. Dinia and D. Lenoble, *Catal. Today*, 2018, **306**, 215–222.
41 S. Teixeira, R. Gurke, H. Eckert, K. Kühn, J. Fauler and G. Cuniberti, *J. Environ. Chem. Eng.*, 2016, **4**, 287–292.
42 N. Serpone and A. Salinaro, *Pure Appl. Chem.*, 1999, **71**, 303–320.
43 S. W. da Silva, J. P. Bortolozzi, E. D. Banús, A. M. Bernardes and M. A. Ulla, *Chem. Eng. J.*, 2016, **283**, 1264–1272.
44 J. R. Bolton, K. G. Bircher, W. Tumas and C. A. Tolman, *Pure Appl. Chem.*, 2001, **73**, 627–637.
45 R. Boppella, K. Anjaneyulu, P. Basak and S. V. Manorama, *J. Phys. Chem. C*, 2013, **117**, 4597–4605.
46 B. Chen, X. Wang, S. Zhang, C. Wei and L. Zhang, *J. Porous Mater.*, 2014, **21**, 1035–1039.
47 A. Benad, F. Jürries, B. Vetter, B. Klemmed, R. Hübner, C. Leyens and A. Eychmüller, *Chem. Mater.*, 2017, **30**, 145–152.
48 W. Li, M. Zhang, J. Zhang and Y. Han, *Front. Chem.*, 2006, **1**, 438–442.
49 H. S. Fogler, *Elements of chemical reaction engineering*, Upper Saddle River, N.J., 3rd edn, 1999.
50 Y. He, N. B. Sutton, H. H. H. Rijnaarts and A. A. M. Langenhoff, *Appl. Catal., B*, 2016, **182**, 132–141.
51 I. Horovitz, D. Avisar, M. A. Baker, R. Grilli, L. Lozzi, D. Di Camillo and H. Mamane, *J. Hazard. Mater.*, 2016, **310**, 98–107.
52 H. Mohan, V. Ramalingam, A. Adithan, K. Natesan, K. K. Seralathan and T. Shin, *J. Hazard. Mater.*, 2021, **416**, 126209.
53 Q. Sun, Z. Li, J. Wang, S. Li, B. Li, L. Jiang, H. Wang, Q. Lü, C. Zhang and W. Liu, *Colloids Surf., A*, 2015, **471**, 54–64.
54 M. Zhao, R. Wang, C. Dai, X. Wu, Y. Wu, Y. Dai and Y. Wu, *Chem. Eng. Sci.*, 2019, **206**, 203–211.
55 A. Ramirez-Canon, M. Medina-Llamas, M. Vezzoli and D. Mattia, *Phys. Chem. Chem. Phys.*, 2018, **20**, 6648–6656.
56 G. Liu, J. C. Yu, G. Q. Lu and H. M. Cheng, *Chem. Commun.*, 2011, **47**, 6763–6783.
57 H. J. Yun, H. Lee, J. B. Joo, W. Kim and J. Yi, *J. Phys. Chem. C*, 2009, **113**, 3050–3055.
58 A. Leelavathi, G. Madras and N. Ravishankar, *Phys. Chem. Chem. Phys.*, 2013, **15**, 10795–10802.
59 M. S. Bakshi, *Cryst. Growth Des.*, 2015, **16**, 1104–1133.
60 A. McLaren, T. Valdes-Solis, G. Li and S. C. Tsang, *J. Am. Chem. Soc.*, 2009, **131**, 12540–12541.
61 Y.-H. Ni, X.-W. Wei, X. Ma and J.-M. Hong, *J. Cryst. Growth*, 2005, **283**, 48–56.
62 Y.-X. Wang, J. Sun, X. Fan and X. Yu, *Ceram. Int.*, 2011, **37**, 3431–3436.
63 R. Chen, W. Jia, D. Lao, S. Li and D. Hei, *J. Alloys Compd.*, 2019, **806**, 596–602.
64 S. Josset, S. Hajiesmaili, D. Begin, D. Edouard, C. Pham-Huu, M. C. Lett, N. Keller and V. Keller, *J. Hazard. Mater.*, 2010, **175**, 372–381.
65 G. Plesch, M. Gorbár, U. F. Vogt, K. Jesenák and M. Vargová, *Mater. Lett.*, 2009, **63**, 461–463.
66 G. Plesch, M. Vargová, U. F. Vogt, M. Gorbár and K. Jesenák, *Mater. Res. Bull.*, 2012, **47**, 1680–1686.
67 N. P. F. Gonçalves, M. A. O. Lourenço, S. R. Baleuri, S. Bianco, P. Jagdale and P. Calza, *J. Environ. Chem. Eng.*, 2022, **10**, 107256.
68 L. Paredes, S. Murgolo, H. Dzinun, M. H. Dzarfan Othman, A. F. Ismail, M. Carballa and G. Mascolo, *Appl. Catal., B*, 2019, **240**, 9–18.
69 A. Surenjan, B. Sambandam, T. Pradeep and L. Philip, *J. Environ. Chem. Eng.*, 2017, **5**, 757–767.
70 J. M. Buriak, P. V. Kamat and K. S. Schanze, *ACS Appl. Mater. Interfaces*, 2014, **6**, 11815–11816.